The Astrophysical Journal, 602:422–435, 2004 February 10

THE ROLE OF MAGNETIC RECONNECTION IN THE OBSERVABLE FEATURES OF SOLAR ERUPTIONS

J. Lin, J. C. Raymond, and A. A. van Ballegooijen
Harvard-Smithsonian Center for Astrophysics, 60 Garden Street, Cambridge, MA 02138
Received 2003 May 16; accepted 2003 October 19

ABSTRACT

There are two competing classes of models for coronal mass ejections (CMEs): those that assume a preexisting magnetic flux rope and those that can make a flux rope during the eruption by magnetic reconnection. The present work is based on the model with a preexisting flux rope. We investigate the evolution of morphological features of the magnetic configuration in a CME according to a catastrophe model of flux rope CMEs developed previously. For the parameters chosen for the present work, roughly half of the total mass and magnetic flux are contained in the initial flux rope, while the remaining plasma and poloidal magnetic flux are brought by magnetic reconnection from the corona into the current sheet and from there into the CME bubble. These features and the corresponding physical processes are identical to those described by the non–flux rope models. Thus, the flux rope and non–flux rope models are less distinct than is generally assumed. The reconnected magnetic flux can account for the rapid expansion of the ejecta, and the plasma flowing out of the current sheet fills the outer shell of the ejecta. We tentatively identify the outer shell, the expanded bubble, and the flux rope with the leading edge, void, and core of the three-component CME structure, respectively. Thus, the final mass, speed, and magnetic energy—the quantities that determine the geoeffectiveness of the CME—are determined not in the initial eruption but during the CME expansion, at heights of a few solar radii. The aspects of this explanation that need improvement are also discussed.

Subject headings: MHD — plasmas — Sun: coronal mass ejections (CMEs) — Sun: filaments — Sun: magnetic fields

1. INTRODUCTION

Solar flares, eruptive prominences, and coronal mass ejections (CMEs) are believed to be different manifestations of a single physical process that involves a disruption of the coronal magnetic field (Harrison 1996; Forbes 2000a). Any attempt to explain solar eruptions has to account for two basic aspects of eruptive processes (Priest & Forbes 2002). The first aspect is the fundamental cause of the eruption itself, and the second is the nature of the morphological features that form and develop during the eruptive process. Such features include the rapid ejections of large amounts of magnetic flux and plasma into interplanetary space, separating bright Hα ribbons on the solar disk, and rising soft X-ray and Hα loop systems in the corona. The catastrophic loss of mechanical equilibrium in a coronal magnetic structure constitutes a fairly promising mechanism for triggering eruptions, and driven magnetic reconnection in the current sheet stretched out by the eruption can cause the subsequent evolution and related features (Forbes 2000b; Lin 2001). There are, however, two competing models for the pre-CME magnetic configuration. Some models (e.g., Forbes & Isenberg 1991; Gibson & Low 1998; Krall, Chen, & Santoro 2000; Wu, Guo, & Dryer 1997; Roussev et al. 2003) assume that a magnetic flux rope above the solar surface becomes unstable as a result of footpoint motion, injection of magnetic helicity, or draining of heavy prominence material. Other models (e.g., Mikić, Barnes, & Schnack 1988; Mikić & Linker 1994; Antiochos, DeVore, & Klimchuk 1999; Amari et al. 2003; Manchester 2003) begin with a sheared magnetic structure that becomes unstable as a result of reconnection (Gosling 1993). The latter models may create a flux rope by reconnection between the sides of the arcade during the eruption process.

Recent work indicates that reconnection during the eruption process is also important for the flux rope models. After finding an analytic description of a magnetic configuration including a current sheet elevated above the solar surface, Lin & Forbes (2000) and Forbes & Lin (2000) studied how magnetic reconnection affects the dynamics and energetics of CMEs, and how the latter in turn affects the former. Their work, together with that of Lin (2001) and Lin, Forbes, & Isenberg (2001), further indicates quantitatively that magnetic reconnection occurring in the coronal magnetic structure does not necessarily play an essential role in *triggering* the catastrophe or initiating eruption, but it does help a catastrophe develop into a plausible eruption, as well as heating the solar atmosphere during the eruption. On the basis of the above works, Lin (2002) studied more details of CME processes in a realistic plasma environment, and the results regarding the dynamic behavior of the current sheet are fairly consistent with observations (see Švestka 1996; Švestka et al. 1997; Švestka & Fárník 1998; Ciaravella et al. 2002; Ko et al. 2003; and Webb et al. 2003).

In addition to the dynamic behavior of the current sheet and ejecta, UVCS observations conducted by Akmal et al. (2001), Ciaravella et al. (2002), and Ko et al. (2003) and *TRACE* observations by Filippov & Koutchmy (2002) show clear evidence of plasma heating of CMEs. The cause of the heating is not clear, but it may be related to magnetic reconnection in the current sheet during the eruption.

Various physical and morphological features that may appear in an eruptive process are illustrated in Figure 1. This scenario is more likely to occur in a major event that manifests a solar flare, an eruptive prominence, and a CME at different stages and spatial locations. During this process, the closed magnetic field in the corona is so stretched by the catastrophic loss of equilibrium of the flux rope (Fig. 1, upper segment of the top panel) that the field effectively opens up and a current sheet forms in the wake of the flux rope, as first proposed by

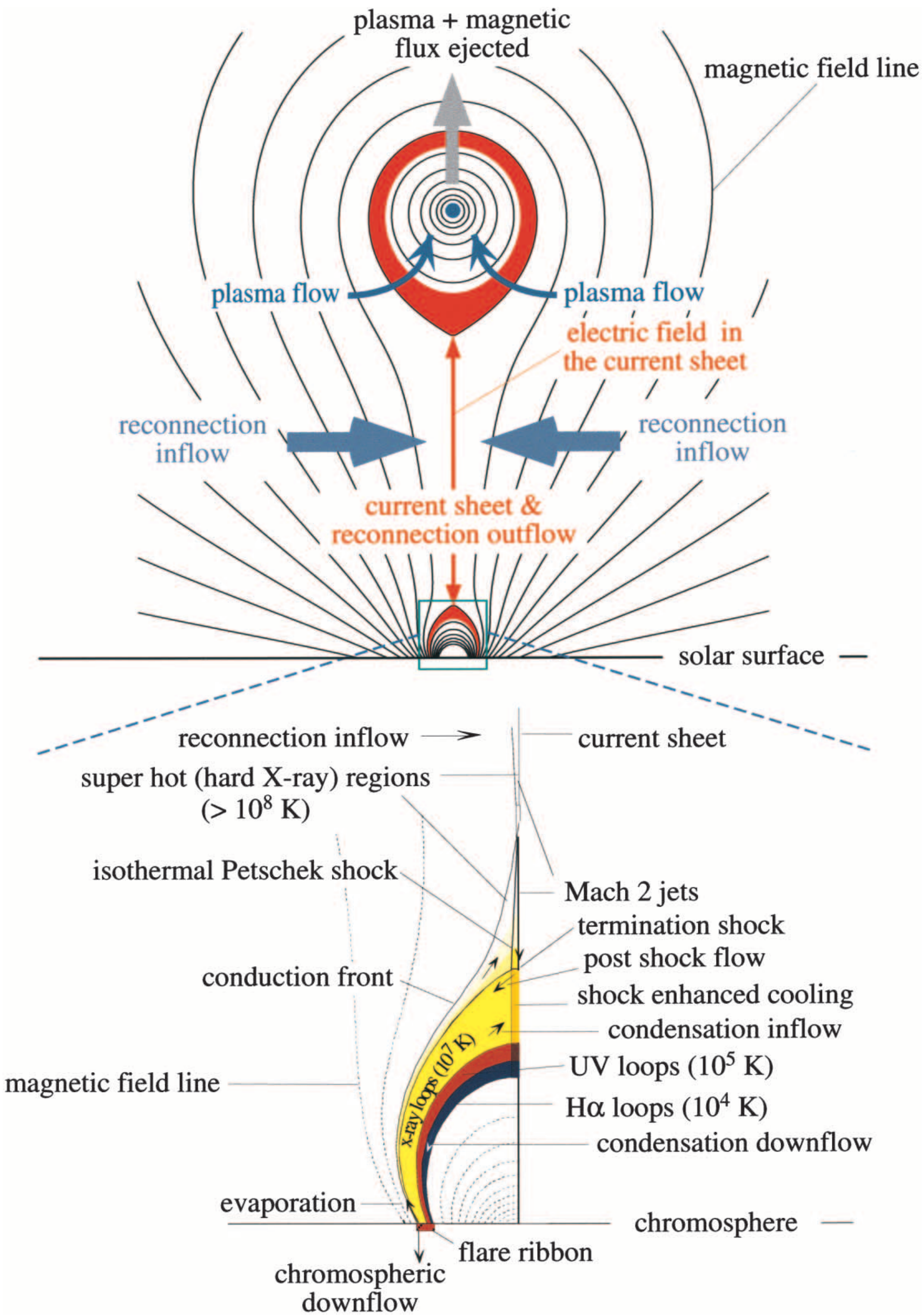

FIG. 1.—Schematic diagram of a disrupted magnetic field that forms in an eruptive process. Colors are used to roughly denote the plasma layers in different temperatures. This diagram incorporates the two-ribbon flare configuration of Forbes & Acton (1996) and the CME configuration of Lin & Forbes (2000).

Carmichael (1964) and Kopp & Pneuman (1976) (Fig. 1, middle segment of the top panel). This concept has been developed into the standard two-ribbon flare model (see Švestka & Cliver 1992 for a review). Magnetic reconnection enabled by plasma instabilities inside the current sheet creates the separating flare ribbons on the solar disk and the growing flare loop systems in the corona (Fig. 1, lower segment of the top panel and enlargement in the bottom panel). Reconnection also helps the extended part of magnetic structure, including the flux rope, escape into the outermost corona and interplanetary space, resulting in a CME (Lin & Forbes 2000; Forbes & Lin 2000). In the remainder of this paper, we reserve the term "flux rope" for the original flux rope that exists prior to the eruption and the term "bubble" for the poloidal flux region that grows around the original flux rope as a result of reconnection.

As indicated by the cartoon in Figure 1, the expanding magnetized plasma bubble surrounding the flux rope (the red shell above the current sheet in the cartoon) is also the product of magnetic reconnection in the current sheet. We propose that the expansion of the bubble is mainly due to the formation of closed or helical field lines around the flux rope, which are successively produced by reconnection. The expansion of the plasma within the bubble may also play a role, but at least during the initial phase of the eruption, the growth of the bubble by reconnection is the dominant process. The reconnected plasma and magnetic flux are sent into the bubble (the region surrounded by the red shell in the top panel of Fig. 1) through the upper tip of the current sheet during the eruption. The successive formation of new closed field lines and the tenuous plasma (density in the range from 10^6 to 10^7 cm^{-3}), as well as the weak magnetic field (strength in the range from 0.1 to 1 G) in the outermost corona, allow the ejected magnetic structure (i.e., the bubble) to expand quickly from a small size (<0.1 solar radius) to a very large size (>1 solar radius) within a short period ($\sim$30 minutes). The expansion of the bubble is also similar to the growth of the flare loop system, which results in the continual transport of magnetic flux from the "open" field to the closed field through the current sheet due to magnetic reconnection (refer to Švestka & Cliver 1992, Forbes & Acton 1996, and Lin, Soon, & Baliunas 2003 for discussions on the CSHKP model [Carmichael 1964; Kopp & Pneuman 1976] for two-ribbon flares) and in the continual propagation of the current sheet onto new field lines (Schmieder et al. 1987). In the framework of catastrophe models, the closed magnetic configuration does not need to open up to infinity during the eruption. Instead it is just highly stretched, and the magnetic field near the lower tip of the current sheet behaves much like that in the totally open configuration. As Figure 1 suggests, the magnetic configuration in the CSHKP model constitutes the low-altitude component of the disrupted magnetic structure in the catastrophe models.

In § 2, we present a model of the system evolution, following the development of the current sheet to investigate the bubble expansion and plasma injection and to study the effect of the reconnected plasma and magnetic flux on CME propagation. In § 3, the total magnetic flux brought by magnetic reconnection from the corona to interplanetary space is computed. The evolution of the bubble and the corresponding observational consequences are worked out in § 4, and the conclusions of our work, together with some discussions on possible speculation based on the present work, are presented in § 5.

2. EFFECT OF RECONNECTED PLASMA MASS ON FLUX ROPE MOTION

Lin & Forbes (2000) constructed a model of solar eruptions. This model consists of a two-dimensional magnetic configuration in the semi-infinite x-y plane, with $y = 0$ being the photospheric boundary (or properly, the base of the corona) and $y > 0$ corresponding to the corona. At any given time t, a force-free flux rope with radius r_0 is located at height h on the y-axis. Below it there may exist an elevated, vertical current sheet along the y-axis, with its lower tip at $y = p$ and upper tip at $y = q$, as shown in Figure 2. The background field in this configuration is produced by two point-source regions on the photosphere, which are separated by a distance of 2λ. The initial quasi-static evolution in the system in response to the slow decrease in λ eventually transits to a dynamic evolution, as a result of the catastrophe when λ reaches the critical value λ_c. The subsequent evolution is rapid compared to the change in the background field. Therefore, λ can be considered unchanged after the catastrophe, and its value is thus fixed at λ_c in calculations of any parameter that describes the eruptive process.

On the basis of this model, we can calculate how much mass is sent into the bubble at any given time. As shown in Figure 1, the plasma that enters the bubble during the eruption has two sources. The first source is the reconnected plasma that is brought by the reconnection inflow (note the thick blue arrows) from the corona near the current sheet and is then sent into the bubble through the current sheet by reconnection. This plasma is heated by reconnection as it passes through the current sheet. The other source is the plasma flow, indicated by the blue curved arrows in Figure 1. This plasma does not go through the current sheet before entering the bubble, but automatically becomes part of the bubble with the formation of new closed magnetic field lines, and therefore it is not heated.

Making use of the formulae and equations deduced by Lin & Forbes (2000) and Lin (2002) for coupling magnetic reconnection to CME propagation and the empirical model of the coronal plasma density given by Sittler & Guhathakurta (1999), the total plasma mass sent into the bubble may be evaluated. In our calculations below, the magnetic field at the origin (refer to Fig. 2) is denoted as B_0, the initial mass m_0 contained by the flux rope is 2.1×10^{16} g, and the average magnetic reconnection rate is approximated by that measured at the center of the current sheet. The rate of magnetic reconnection is given by the inflow speed near the current sheet in units of the local Alfvén speed, the Alfvén Mach number M_A.

In principle, M_A varies with time and the properties of the plasma and magnetic field near the reconnection site, such as the length and thickness of the current sheet, strength of the magnetic field, and plasma resistivity. Since there is no generally accepted, rigorous theory for how fast reconnection occurs when driven by a catastrophic loss of equilibrium, we assume that M_A is a constant less than unity and take $M_A = 0.1$ in the following calculations. For detailed discussions of the functional behavior and plausible values of M_A, see Lin & Forbes (2000) and Forbes & Lin (2000).

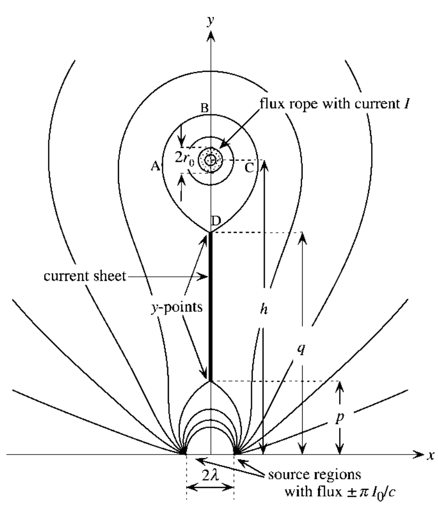

FIG. 2.—Diagram of the CME/flux rope configuration, showing the mathematical notations used in the text (from Lin & Forbes 2000). The height of the center of flux rope is denoted by h, p and q denote the lower and the upper tips of the current sheet, respectively, and the distance between the magnetic source regions on the photosphere is 2λ.

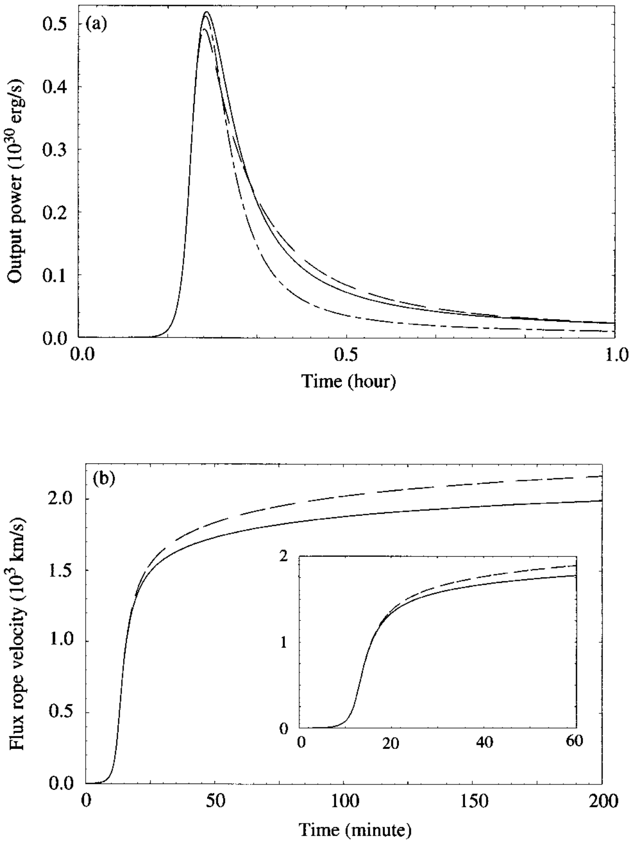

FIG. 3.—Results of calculations for justifying some approximations and modifications made in the present work. (*a*) Output powers of eruptive process, corresponding to where the rate of reconnection is evaluated along the current sheet: at the center of the current sheet (*solid curve*) and at the center of the lower half-section (*dashed curve*) and upper half-section of the current sheet (*dot-dashed curve*). (*b*) Effect of the mass of ejecta on CME propagation velocities. The solid curve is for the case in which the mass of ejecta changes during eruption and the dashed curve for the case of fixed mass.

To justify the use of the magnetic reconnection rate measured at the midpoint of the current sheet to approximate the average rate of magnetic reconnection during the eruptive process in our calculations, Figure 3*a* gives the output power P of the eruptive process against time for $B_0 = 100$ G, evaluated as

$$P = m\dot{h}\frac{d\dot{h}}{dt}, \qquad (1)$$

where $\dot{h}$ is velocity of the ejecta. The solid curve corresponds to evaluating the reconnection rate at the center of the current sheet; the dashed curve corresponds to the rate at a quarter of $q-p$ from the lower tip of the current sheet, and the dot-dashed curve to the rate at the same distance from the upper tip of the current sheet. Obviously, they are not very different, and the difference between the solid curve and the average of the two others is very small. Therefore, our approximation for the rate of magnetic reconnection during the eruptive process can be considered reasonable.

Successive reconnection keeps sending extra plasma into the bubble that moves together with the flux rope, increasing the total mass inside the bubble. This extra mass could, more or less, affect the motions of the flux rope and the bubble as a whole. Figure 3*b* plots velocities of the flux rope $\dot{h}$ against time t for $B_0 = 100$ G in the cases of fixed total mass $m = m_0$ and increasing total mass. It does not show a substantial difference. This implies that the extra mass sent into the separatrix bubble by reconnection does not affect CME motions significantly, at least for the cases studied in the present work (strong magnetic field, 100 G, at the photospheric surface and fast CME).

The total amount of plasma injected into the bubble is given in Figure 4 for background fields of different strengths. (Here we assume that the system extent in z-direction, L, is 10^5 km; see Lin & Forbes 2000.) The total added mass varies from 1.92×10^{16} to 2.14×10^{16} g, depending on the strength of the relevant background field. Compared with the initial mass inside the flux rope, $m_0L = 2.1 \times 10^{16}$ g, the total mass in the separatrix bubble increases as a result of reconnection by about 100% (in the range 92%–102%). Figure 4 also suggests that the amount of reconnected plasma increases somewhat with the strength of the background field and that most of the reconnected mass comes from the low corona. The increase in mass with magnetic field strength is because plasma is brought to the reconnection site at a rate proportional to the local Alfvén speed and is thus roughly proportional to the background field. The added material mostly originates in the low corona, because the plasma is denser at the lower altitudes. An important conclusion from Figures 3*b* and 4 is that plenty of plasma is brought by the eruption from the corona to interplanetary space, but the increase of the mass during CME propagation does not significantly affect the dynamical behavior of CME, because the whole process is controlled by the magnetic field.

The plots in Figure 4 also imply that although most of the mass (~80%) due to reconnection is added within the first 1 to ~1.5 hr after the onset of reconnection, the mass within the CME keeps increasing over a long period of time. This means that the average masses of CMEs derived from the traditional coronagraph data near the Sun are underestimated. The older coronagraph data gave a few times 10^{15} g for the masses carried away by CMEs (Howard et al. 1985; Hundhausen, Stanger, & Serbicki 1994). Studies using *Helios* (Webb, Howard, & Jackson 1996) and LASCO (Howard et al. 1997) indicated that the above masses were underestimated by factors of 3–10, probably because mass outflow can continue well after the CME's leading edge leaves the instrument field of view (Webb 2000). Most recently, Ko et al. (2003) investigated a CME that leaves a long, thin, streamer-like structure

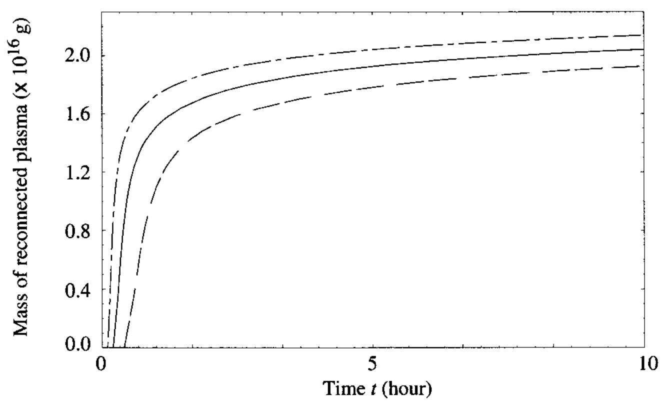

FIG. 4.—Variations of the amount of reconnected plasma vs. time for different background fields: $B_0 = 50$ G (*dashed curve*), 100 G (*solid curve*), and 200 G (*dot-dashed curve*).

behind. The high ionization state of the plasma ([Fe XVIII] emission is observed) inside this structure and a growing flare/CME loop system in EIT 195 Å right beneath it indicate that it is the current sheet that develops in a disrupted magnetic field according to the model of Lin & Forbes (2000). The continuous plasma outflow along the current sheet observed by Ko et al. (2003) seems to endorse Webb's (2000) conclusion and our result.

3. MAGNETIC FLUX EJECTED INTO INTERPLANETARY SPACE

Basically, the magnetic flux that is brought into the outermost corona and interplanetary space by the CME may consist of three parts (see Fig. 5). The first part exists inside the flux rope (inside the innermost green contour in Fig. 5). The second part is due to the magnetic field lines in the bubble surrounding the flux rope (Fig. 5, *green contours*). In the two-dimensional model, these field lines are closed curves, but they are quite likely to spiral and connect to the solar surface, as in the configuration investigated by Lin, van Ballegooijen, & Forbes (2002). The third component of ejected flux comes from those field lines that pass over the flux rope and are anchored in the photosphere at the both ends (*blue contours*). Generally, all three components of magnetic flux include both poloidal and toroidal field. According to the theoretical models of flux rope (prominence) formation, both the first and second components of magnetic flux depend on how the flux rope is created (for theoretical models of flux rope formation, see van Ballegooijen & Martens 1989, Choe & Lee 1992, Inhester, Birn, & Messe 1992, Amari et al. 2000, Aulanier, Srivastava, & Martin 2000, van Ballegooijen, Priest, & Mackay 2000, and Mackay & van Ballegooijen 2001).

In general, the three magnetic flux components are not easily distinguishable observationally, although perhaps it is possible to distinguish them on the basis of plasma composition. Within the framework of the catastrophe model, all the toroidal fields are assumed to be confined inside the flux rope, and the magnetic field outside the flux rope is poloidal in order to simplify some essential integrals for the analytic solutions (see Forbes & Isenberg 1991). This gives rise to an artificial distinction between the first and second parts of magnetic flux. In some other CME models, such as the shearing arcade (Mikić & Linker 1994) and breakout (Antiochos et al. 1999) models, no flux rope exists prior to the eruption, so the first component of magnetic flux mentioned above is absent.

As shown in Figure 5, the green and blue magnetic field lines (those inside the flux rope are not drawn) have different topological connections, and they are separated by the separatrix (*red field line*). This special field line forms two T-type neutral points on the surface, but no dissipation occurs because of the line-tying condition on the surface. Strictly speaking, the red line cannot be recognized as the separatrix before connecting to an X-type neutral point or a current sheet. Wang (1998) suggests an alternative term, magnetic interface, to distinguish the magnetic boundaries on which no reconnection or dissipation occurs from those on which reconnection occurs (see also the discussions by Wang 1999 and Lin & Wang 2002). As two T-points merge to form an X-point during the evolution of the configuration, the magnetic interface develops into a separatrix in the normal sense, and reconnection starts turning the blue field lines into green ones. Therefore, the amount of magnetic flux due to the blue field lines constitutes the total amount of the magnetic flux that can be brought from the corona by magnetic reconnection and sealed into the separatrix bubble (see the red shell surrounding the flux rope in Fig. 1) via the upper tip of the current sheet during the eruption. Denoting this amount of flux as $\Phi_{\rm photo}$, we have

$$\Phi_{\rm photo} = \frac{I_0 \pi}{c} L \tag{2}$$

(see Forbes & Priest 1995), where I_0 is a constant with the dimensions of electric current intensity. It is related to B_0 by

$$B_0 = \frac{2I_0}{c\lambda_0}$$

and $\lambda_0 = 5 \times 10^4$ km, which is one-half of the value of the typical length of active regions. In our calculations below, λ_0 is used to normalize other lengths.

In the current analytic frame of the catastrophic models, the magnetic fluxes due to the green and blue field lines (Fig. 5) can be uniquely determined for a given magnetic configuration, while the flux inside the flux rope has some arbitrariness. This is because we are using the thin–flux rope approach in these models to decouple the internal and external magnetic fields, in order to find analytic solutions for the problem (see also Forbes & Isenberg 1991 for more details). In this case, the interior structure of the flux rope is not very essential for the global behavior of the system, which depends only on the total current intensity $\tilde{I}$ in the flux rope. This is related to the radius of flux rope, r_0, by

$$r_0 = r_{00}/\tilde{I}, \tag{3}$$

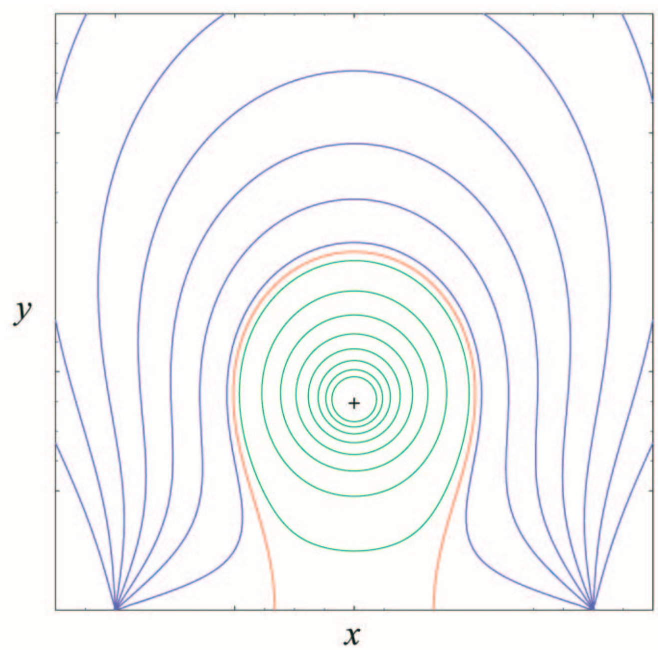

FIG. 5.—Schematic diagram of magnetic flux systems with different topological connections. Blue curves describe the field lines passing over the flux rope and connecting two source regions on the boundary surface, green curves are for field lines surrounding the flux rope and connecting to themselves, and the red curve specifies a special field line and also a boundary known as the magnetic interface that separates the magnetic flux systems of different topological connections. The cross indicates the center of the flux rope.

where $\tilde{I}$ is the total current inside the flux rope in units of I_0, and r_{00} is the value of r_0 for $\tilde{I} = 1$. This relation of r_0 to $\tilde{I}$ has been extensively used in our previous works (Lin et al. 1998, 2001, 2002; Lin & Forbes 2000; Lin 2001, 2002; and Lin & van Ballegooijen 2002). It is an approximation of Parker's (1974) exact solution of force-free magnetic field in the flux rope, which is an implicit and transcendental relation and is thus cumbersome to use. We see below that this relation can also be deduced from the Lundquist (1950) solution for a force-free field. We refer interested readers to the work of Forbes & Priest (1995) and Lin et al. (1998) for further clarification and discussion.

To estimate the magnetic flux inside the flux rope, we assume that the magnetic field in the flux rope is described by the Lundquist (1950) solution as one of the many possible choices:

$$B_r = 0, \quad B_\phi = H_0 J_1(\alpha r), \quad B_z = H_0 J_0(\alpha r), \tag{4}$$

where α is the force-free factor and is constant, r is the radial distance from the axis of flux rope, and we have $r \leq r_0$ for this equation, as well as the other relevant equations. Hereafter, J_0 and J_1 are Bessel functions of the first kind, and H_0 is the magnetic field strength on the flux rope axis. In fact, observers also use the Lundquist solution to fit their data obtained for magnetic clouds (flux ropes) at 1 AU (Burlaga 1988; Lepping, Jones, & Burlaga 1990). The force-free configuration inside the flux rope described by equation (4) is well maintained at 1 AU, and the internal magnetic field is apparently stronger than that outside.

To maintain a current-free magnetic field outside the flux rope, we require that B_z vanish and $B_\phi = 2I/cr$ outside the flux rope, namely,

$$B_r = 0, \tag{5a}$$

$$B_\phi = H_0 J_1(\alpha r_0) = \frac{2I}{cr_0}, \tag{5b}$$

$$B_z = H_0 J_0(\alpha r_0) = 0, \tag{5c}$$

at $r = r_0$, the surface of the flux rope. Here, the total current intensity I is related to $\tilde{I}$ and I_0 by $I = \tilde{I} I_0$. Equation (5b) leads to

$$H_0 = (2I/cr_0)/J_1(\alpha r_0), \tag{6}$$

and equation (5c) gives

$$\alpha r_0 = x_0 \text{ or } \alpha = x_0/r_0, \tag{7}$$

where x_0 is the first zero of $J_0(x)$, which is 2.4048. Substituting H_0 and α into equation (4) yields

$$B_r = 0, \quad B_\phi = \frac{2I}{cr_0}\frac{J_1(rx_0/r_0)}{J_1(x_0)}, \quad B_z = \frac{2I}{cr_0}\frac{J_0(rx_0/r_0)}{J_1(x_0)}. \tag{8}$$

Thus, the magnetic flux due to B_ϕ is

$$\Phi_{\rm pol} = \frac{2I}{cr_0} l \int_0^{r_0} \frac{J_1(\alpha r)}{J_1(x_0)}\, dr = \frac{2I_0}{cx_0 J_1(x_0)}\tilde{I} l, \tag{9}$$

and that due to B_z is

$$\Phi_{\rm tor} = \frac{4\pi I}{cr_0}\int_0^{r_0} \frac{J_0(\alpha r)}{J_1(x_0)} r\, dr = \frac{4\pi I}{c\alpha}, \tag{10}$$

where l is the length of the flux rope, and prior to the eruption it is the extent of the system in the z-direction, L, which is of the order of 10^5 km.

From equation (7), we find that setting $\Phi_{\rm tor} = $ const in equation (10) simply leads to $r_0 I = $ const, which just yields equation (3). (The conservation of $\Phi_{\rm tor}$ is discussed in the Appendix.) Applying the known relations deduced earlier to equation (10), we find

$$\Phi_{\rm tor} = \frac{4\pi I_0 \tilde{I} r_0}{cx_0} = \frac{4\pi I_0 r_{00}}{cx_0} = 2\pi B_0 \frac{r_{00}\lambda_0}{x_0}$$

and $\Phi_{\rm tor} = 6.53 \times 10^{20}$ Mx for $B_0 = 100$ G and $r_{00} = 0.1\lambda_0 = 5000$ km. The value of $\Phi_{\rm tor}$ deduced here is comparable to the observational results obtained by Lepping et al. (1997) and Vourlidas et al. (2000), which are 7.5×10^{20} and 1.3×10^{21} Mx on average, respectively.

It is more difficult to obtain a reasonable estimate for $\Phi_{\rm pol}$. Equation (9) indicates that $\Phi_{\rm pol}$ varies linearly with both l and $\tilde{I}$. In the two-dimensional regime, l is the length of the flux rope in z-direction and remains equal to the constant, L. In reality, however, the two-dimensional description may be valid only when the flux rope height h remains less than its length l. As long as $h \leq l$ holds, l can roughly remain equal to L, and the current $\tilde{I}$ decreases as the flux rope ascends (refer to the formulations of Lin & Forbes 2000 for more details regarding variations of $\tilde{I}$ vs. h). When h exceeds L, the flux rope will be significantly stretched, l will increase with time, and the flux rope may then expand self-similarly. The increase in l is thus quite likely to compensate the decrease in $\tilde{I}$ during the self-similar evolution, so that $\Phi_{\rm pol}$ given in equation (9) may remain more or less unchanged. On this basis, an estimate of $\Phi_{\rm pol}$ can be made. For $B_0 = 100$ G, at the time when $h = l = L$, $\tilde{I}$ is given by equation (18) of Lin & Forbes (2000), and we find that $\tilde{I} = 0.92$. Substituting this value of $\tilde{I}$ into equation (9) gives $\Phi_{\rm pol} = 3.69 \times 10^{21}$ Mx. Note that $\Phi_{\rm pol}$ is significantly larger than $\Phi_{\rm tor}$.

We are able to calculate the magnetic flux due to the green field lines (we denote it as Φ_{o1} hereafter), as shown in Figure 5, by evaluating the flux function $A(x, y)$ on the surfaces of the flux rope and the boundary at $t = 0$. Here $A(x, y)$ is related to magnetic field $\boldsymbol{B}(x, y)$ by $\boldsymbol{B}(x, y) = \nabla A(x, y) \times \hat{z}$, and $\hat{z}$ is the unit vector in the z-direction. Because $A(x, y)$ depends on flux rope height h, current sheet parameters p and q, and other functions of time t, we need to keep in mind that $A(x, y)$ varies with time as well, although t does not explicitly appear in the expressions for $A(x, y)$. According to Forbes & Priest (1995), the poloidal magnetic flux before initiation of reconnection, Φ_{o1}, is equal to $L[A(0, h - r_0) - A(0, 0)]$, where $A(0, h - r_0)$ is the value of $A(x, y)$ at the surface of the flux rope and $A(0, 0)$ that at the boundary surface (refer to Figs. 2 and 5). Thus, we find

$$\Phi_{o1} = L\left\{\frac{I_0}{c}\left[2\ln\left(\frac{2}{r_{00}}\right) + \frac{\pi}{2}\right] - \frac{I_0}{c}\pi\right\} = B_0\lambda_0 L\left[\ln\left(\frac{2}{r_{00}}\right) - \frac{\pi}{4}\right], \tag{11}$$

according to equation (2.5) of Forbes & Priest (1995). The value of Φ_{o1} in equation (11) does not change until reconnection commences at $t = t^*$, when a neutral point appears at the boundary surface and a current sheet starts to develop (refer to Lin & Forbes 2000 and Lin 2002 for more discussions). In our system, $\Phi_{o1} = 1.11 \times 10^{22}$ Mx for $B_0 = 100$ G. However, comparing this value with observations may not be easy, because we do not have a method for coronal magnetography. An in situ measurement can only provide a total amount of the poloidal flux that includes the contribution from $\Phi_{\rm pol}$ and Φ_{o2}, which is discussed below.

As reconnection starts ($t \geq t^*$), more and more plasma and magnetic flux are sealed into the separatrix bubble (see the red shell surrounding the flux rope in Fig. 1) via the upper tip of the current sheet from the blue field lines shown in Figure 5. This magnetic flux, which is denoted as Φ_{o2} hereafter, equals the difference of three parameters, $A(0, h - r_0)$, $A(0, q)$, and Φ_{o1}, such that

$$\begin{aligned}\Phi_{o2} &= [A(0, h - r_0) - A(0, q)]L - \Phi_{o1} \\ &= L\left[\frac{I_0 \pi}{c} - A(0, q)\right], \end{aligned} \tag{12}$$

where $A(0, q)$ is actually the value of $A(x, y)$ at the upper tip of the current sheet, which according to Lin & Forbes (2000; eq. [25] for A_0^0) is

$$\begin{aligned}A(0, q) = &\frac{2I_0}{c}\frac{\lambda}{qL_1}\left[(h^2 - q^2)K\left(\frac{p}{q}\right)\right. \\ &\left. + (q^2 - p^2)\Pi\left(\frac{\lambda^2 + p^2}{\lambda^2 + q^2}, \frac{p}{q}\right) - \frac{H_1^2}{h^2}\Pi\left(\frac{p^2}{h^2}, \frac{p}{q}\right)\right].\end{aligned} \tag{13}$$

Here $H_1^2 = (h^2 - p^2)(h^2 - q^2)$ and $L_1^2 = (\lambda^2 + p^2)(\lambda^2 + q^2)$, and K and Π are the complete elliptic integrals of the first and third kinds, respectively. On the basis of the results for h, $\dot{h}$, p, q, and m, we are able to determine $A(0, q)$ in equation (13) as a function of time t. Substituting the resulting $A(0, q)$ into equation (12), we obtain Φ_{o2} as a function of t. Figure 6 plots Φ_{o2} versus t for $B_0 = 100$ G. The total magnetic flux brought into interplanetary space by reconnection in the whole process (lasting up to 20 hr) is about 5.6×10^{21} Mx, which is comparable to $\Phi_{\rm photo} = 7.85 \times 10^{21}$ Mx, according to equation (2). This makes sense, because all blue field lines have to be reconnected in the eruptive process as $t \to \infty$.

However, it seems strange that the total poloidal flux in the initial state, $\Phi_{\rm pol} + \Phi_{o1}$, is larger than $\Phi_{\rm photo}$. This puzzle can actually be resolved by noticing that the formation of the flux rope and the consequent evolution in the system are relatively independent of one another in the regime of the catastrophe models of eruptions. The flux rope is a prerequisite of the catastrophe models. It can be created by reconnection of the footpoints in a sheared magnetic arcade (van Ballegooijen & Martens 1989; Choe & Lee 1992; Inhester et al. 1992; Amari et al. 2000; Aulanier et al. 2000; van Ballegooijen et al. 2000; Mackay & van Ballegooijen 2001), or it can directly emerge from the convective zone into the corona (see Lites et al. 1995; Gibson et al. 2002). Therefore, as the system begins to evolve toward the eruption under the framework of the catastrophe model, the total poloidal flux $\Phi_{\rm pol} + \Phi_{o1}$ is not necessarily related to $\Phi_{\rm photo}$.

On the other hand, $\Phi_{\rm pol} + \Phi_{o1}$ is related to $\Phi_{\rm photo}$ in the shearing arcade model (Mikić & Linker 1994) and the breakout model (Antiochos et al. 1999). In these models, the magnetic configuration does not contain the flux rope or the magnetic flux associated with the green field lines shown in Figure 5, but only the magnetic flux, $\Phi_{\rm photo}$, associated with the blue field lines. Shearing at the footpoints turns part of the poloidal flux in $\Phi_{\rm photo}$ into $\Phi_{\rm tor}$. Thus, the value of $\Phi_{\rm photo}$ may include contributions from both preexisting poloidal components and toroidal components due to shearing, although $\Phi_{\rm photo}$ remains unchanged before reconnection begins. As reconnection starts in the current sheet, new components of the poloidal flux $\Phi_{\rm pol}$, Φ_{o1} and Φ_{o2}, are produced from $\Phi_{\rm photo}$. Therefore, the sum of $\Phi_{\rm tor}$, $\Phi_{\rm pol}$, Φ_{o1}, and Φ_{o2} should not exceed the initial $\Phi_{\rm photo}$ in the models of shearing arcade and breakout. Comparing with the features manifested by the catastrophe model, one may notice that all these three models result in quite similar evolutionary behaviors of CMEs in the eruptive process and that the main difference among them lies in how the formation of the flux rope is included in the system's evolution.

Unlike Φ_{o1}, the value of Φ_{o2} can be determined from observations of flare loops and ribbons. In magnetic reconnection process, the magnetic fluxes flowing from each end of the current sheet must be equal even if the rate of reconnection along the current sheet is not necessarily uniform. The reason is that the magnetic flux outside the reconnection site must be conserved and the divergence-free condition of the magnetic field should be guaranteed everywhere. Therefore, the amount of magnetic flux, Φ_{o2}, that is sent into interplanetary space through the upper tip of the current sheet equals that associated with flare loops and ribbons. Forbes & Lin (2000) point out that the eruption leads to the closed field lines being stretched or transiently extended. This causes the volume of the magnetic structure to increase and plasma density in this structure to decrease quickly, strongly depletes the coronal emission, and forms dimming regions on the solar disk (refer to Figs. 1 and 2 of Forbes & Lin 2000). For a brief review of observations of the dimming phenomenon, see Harrison & Lyons (2000), and for individual studies see Sterling & Hudson (1997), Harrison (1997), Zarro et al. (1999), Thompson et al. (2000), Harrison et al. (2003), and references therein. The dimming areas eventually disappear with appearance of flare ribbons and formation of newly closed flare loops. Since both flare ribbons and loops are the products of magnetic reconnection (see, e.g.,

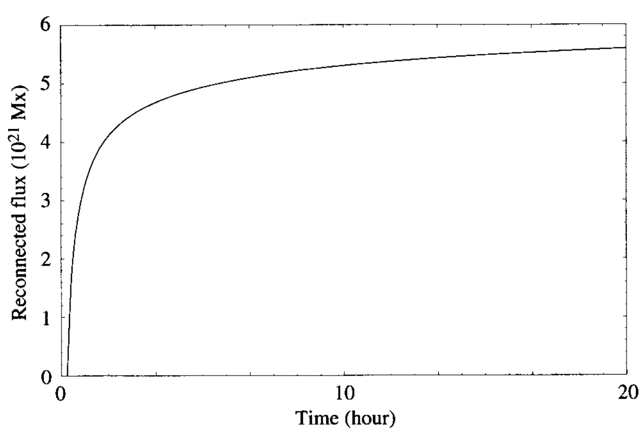

FIG. 6.—Variations of the total magnetic flux sent into interplanetary space by reconnection vs. time for $B_0 = 100$ G.

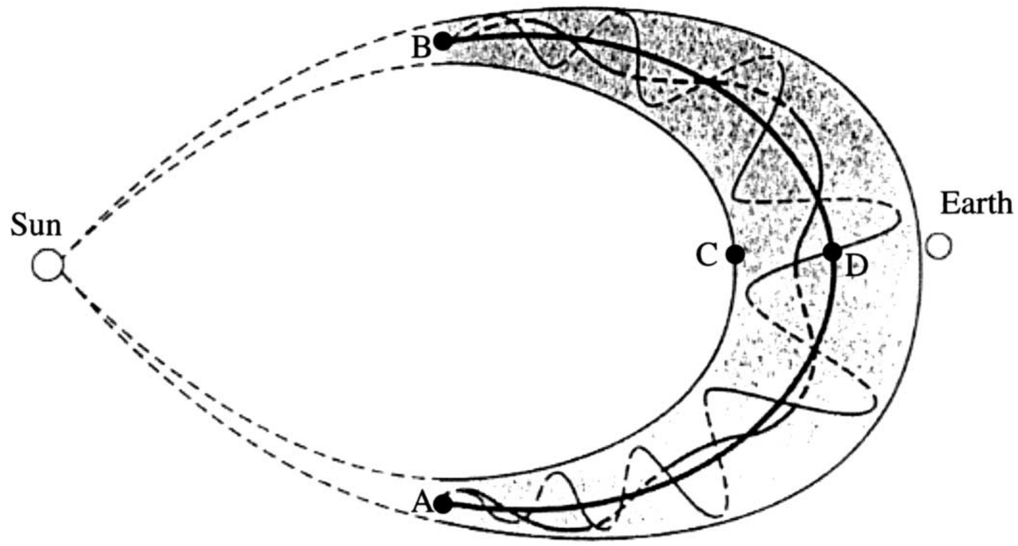

FIG. 7.—Schematic description of how the in situ measurement of the poloidal magnetic flux is conducted. The original template is from Lepping et al. (1997).

Švestka & Cliver 1992; Lin et al. 1995; Forbes & Acton 1996; Priest & Forbes 2002), it is reasonable to believe that the magnetic flux involved in the formation of ribbons and loops should be identical to that in the dimming area.

The bright flare ribbons may not completely cover the dimming areas, because their brightness depends on how much magnetic energy is transported from the reconnection site to the lower atmosphere. With the current sheet moving to higher altitudes, where there is less available magnetic energy, the energy transported downward may not be enough to create bright ribbons. Thus, the flare ribbons may not reach the outer edge of the dimming regions. Therefore, it is more reliable to use the magnetic flux inside the dimming area to evaluate Φ_{o2} than to use the area of flare ribbons. The estimate by Webb et al. (2000) for a specific eruption is about 10^{21} Mx. Comparing this value with that deduced from Figure 6 suggests the consistency of the theory with the observations.

When the flux rope and bubble (or the magnetic cloud, as usually termed by geophysicists) approach the Earth, the total poloidal magnetic flux transported from the Sun by the eruptive process can be determined via in situ measurements. This total flux equals the sum of $\Phi_{\rm pol}$, Φ_{o1}, and Φ_{o2} in our model. We denote it by Φ_S, and the theoretical value of Φ_S according to our calculations above is 2.02×10^{22} Mx. Observations indicate that the magnetic field configuration of a magnetic cloud at 1 AU is force-free to a very good approximation (Goldstein 1983; Marubashi 1986). The geometry of the cloud is a nested set of helical field lines confined to the flux rope, which is curved on a large scale (Farrugia, Burlaga, & Lepping 1997), whose footpoints are anchored back to the Sun for a while (Fig. 7[1]). The field inside the flux rope is approximated by the Lundquist solution (Burlaga 1988; Lepping et al. 1990), and the poloidal flux is

$$\Phi_S = \bar{l} \int_0^{r_0} B_\phi(r)\, dr, \tag{14}$$

where B_ϕ is given in equation (8). Substituting equation (8) into equation (14) leads to

$$\Phi_S = \bar{l} \int_0^{r_0} \frac{2I}{cr_0} \frac{J_1(rx_0/r_0)}{J_1(x_0)}\, dr = \frac{2I}{cx_0} \frac{\bar{l}}{J_1(x_0)} = H_0 \frac{r_0 \bar{l}}{x_0}, \tag{15}$$

where H_0 is given in equation (6), r_0 is the radius of the flux rope, which equals the distance between points C and D, and $\bar{l}$ is the effective length of the magnetic cloud, which is measured along the arc ADB (Fig. 7). Here the contribution to Φ_S from the legs of the flux rope is neglected, because most of the twist is expected to reside in the weak outer part of the flux rope (Parker 1974; also Priest 1982). The in situ measurements give the toroidal field inside the magnetic cloud, H_0, from 15 to 30 nT (or from 1.5×10^{-4} to 3.0×10^{-4} G), and r_0 varies from 0.1 to 0.4 AU (Lepping et al. 1990, 1997; Webb et al. 2000). Taking $\bar{l}$ in the range from 1 to π AU, we get from equation (15) that Φ_S varies from 1.39×10^{21} to 3.52×10^{22} Mx. Similarly, we can also estimate $\Phi_{\rm tor}$ on the basis of the in situ measurements. According to equations (4) and (10), we have

$$\Phi_{\rm tor} = 2\pi \int_0^{r_0} B_z(r) r\, dr = 2\pi H_0 r_0^2 J_1(x_0)/x_0, \tag{16}$$

which brings $\Phi_{\rm tor}$ to the range from 4.55×10^{20} to 1.46×10^{22} Mx. Comparing the values deduced on the basis of in situ measurements with our theoretical calculation indicates good agreement.

4. EVOLUTION OF THE SEPARATRIX BUBBLE

In this section, we look into the behavior of the separatrix bubble (the region surrounded by the red shell at the upper part of Fig. 1) that is attached to the upper tip of the current sheet. As in the flare/CME loop/giant arch system below the current sheet, the evolution of the bubble results directly from the magnetic reconnection. While coronal magnetic field and plasma are being continuously reconnected through the current sheet, the newly formed closed field lines, both those anchored in the photosphere for flare loops and those sur-

[1] The original template for Fig. 7 is from Lepping et al. (1997), and it is also available at http://umbra.nascom.nasa.gov/istp/cloud_talk.html.

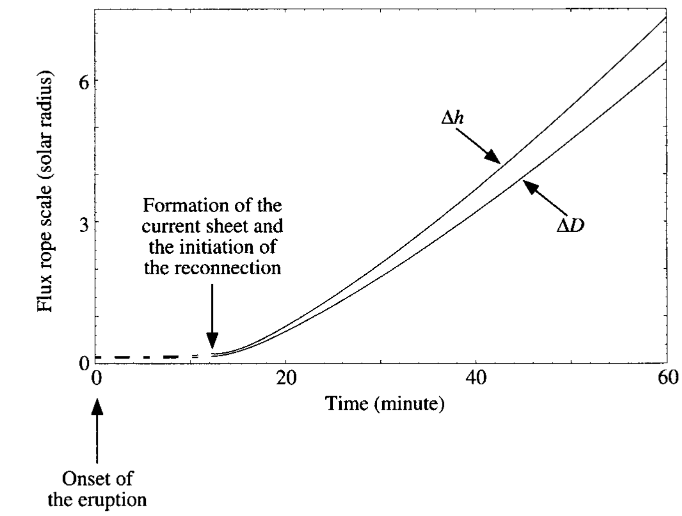

FIG. 8*a*

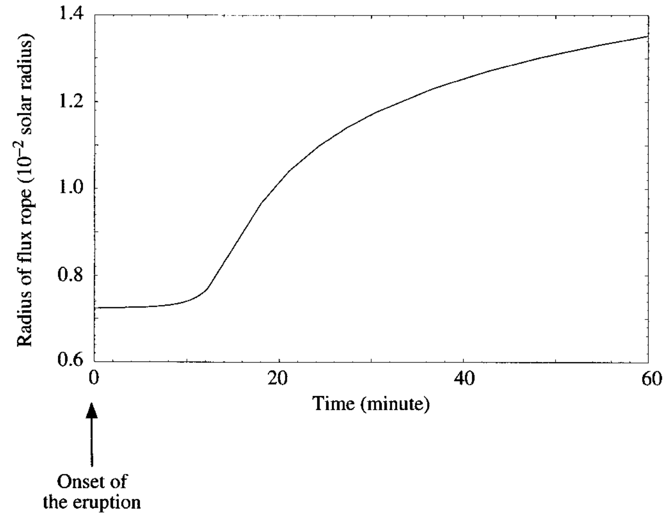

FIG. 8*b*

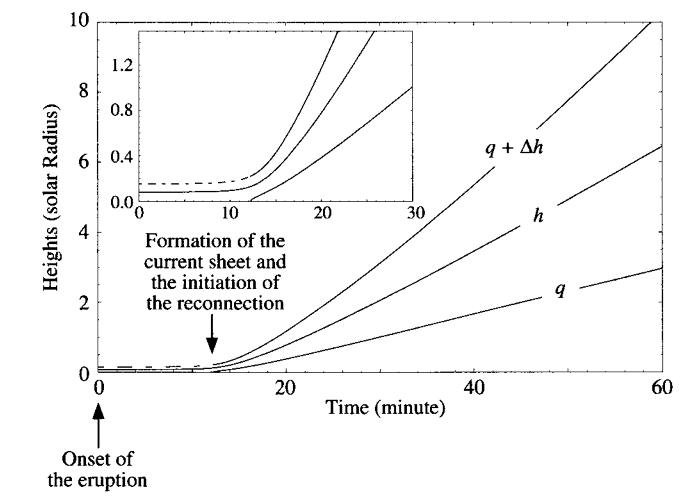

FIG. 8*c*

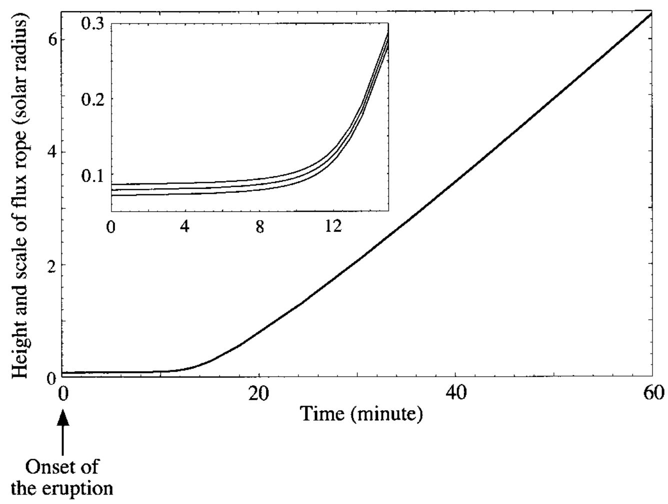

FIG. 8*d*

FIG. 8.—Evolution of the flux rope scale and the morphological features of the separatrix bubble for $B_0 = 100$ G. (*a*) Variations of ΔD and Δh vs. time. The dashed section indicates the stage before reconnection is invoked. (*b*) Variation of the flux rope radius, r_0, vs. time. (*c*) Evolution of the parameters for morphological features of the separatrix bubble. The dashed section indicates the stage before reconnection starts. (*d*) Evolution of the flux rope scale. The inset shows more details: the upper curve is for $h + r_0$, the lower curve is for $h - r_0$, and the middle is for h.

rounding the flux rope, are progressively produced, causing both the flare loop system and the bubble to expand. Compared to the flux rope expansion, which is governed by the internal balance of the flux rope itself (e.g., eq. [3]), the bubble expansion is rapid. In the following subsections, we investigate the evolution of the morphological features of the separatrix bubble and discuss the implications of this evolution for the three-component structure of CMEs separately.

4.1. *Morphological Features of the Separatrix Bubble*

As shown by Figure 2, the size of the bubble can be described by either ΔD, the span between points A and C, and or Δh, the span between points B and D. Because of the cusp structure near the tip of the current sheet, the scale of the bubble in y-direction, Δh, is slightly larger than that in x-direction, ΔD. From the results for h, p, and q, we can determine the magnetic structure of the system at any given time, as shown in Figure 8*a*. The corresponding time profile of the flux rope radius, r_0, is shown in Figure 8*b* according to equation (3). For the purpose of comparison, we also plot h, $q + \Delta h$ (the height of the separatrix bubble apex, B; refer to Fig. 2), and q (the height of the separatrix bubble bottom, D) versus time in Figure 8*c* and time variations of h and $h \pm r_0$ in Figure 8*d*. Obviously, the variation of r_0 versus time is quite different and slower than those of ΔD and Δh.

Figure 9 shows a series of snapshots of the magnetic configuration at different times after the onset of the eruption. The eruption begins with the catastrophic loss of equilibrium in the system at $t = 0$. The configuration does not contain an X-type neutral point or a current sheet above the boundary surface until around 12 minutes (for $B_0 = 100$ G) after the catastrophe occurs (see the discussions of Lin & Forbes 2000 and Lin 2002). Then the reconnected and heated plasma begins to be injected into the separatrix bubble. The volume of the bubble increases as the reconnection proceeds, sending more and more reconnected magnetic flux and plasma into the bubble (see the other panels in Fig. 9 and also the curves in Fig. 8*a*). As indicated by the top panel in Figure 1, the freezing-in of plasma to the magnetic field implies that the reconnected plasma and any associated thermal conduction flux can only be transported through the separatrices. The closed field lines detached from the current sheet prevent the hot plasma from

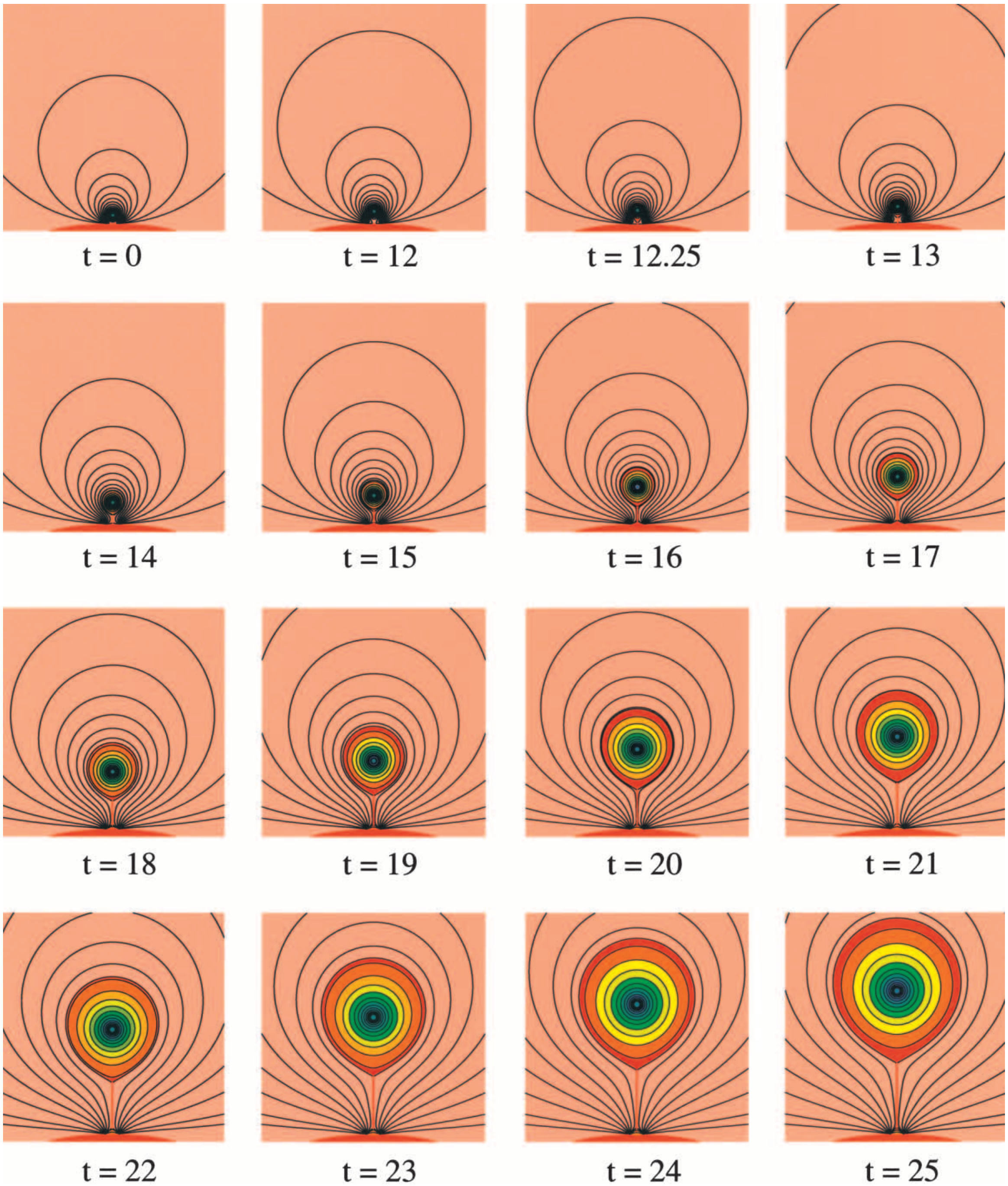

FIG. 9.—Snapshots of the disrupted magnetic configuration at different times after the onset of the eruption for $\sigma = 1$. The eruption is triggered by the catastrophic loss of equilibrium in the system at $t = 0$, an X-type neutral point appears at the boundary surface, and a current sheet starts to develop from the neutral point at $t = 12.21$ minutes; thereafter, the flare/CME loops grows and the separatrix bubble expands.

entering the interior of the separatrix bubble. Without continued heating, the internal plasma starts to cool as a result of the adiabatic expansion and/or radiation. Therefore, the bubble's outer shell is hotter than its internal part, and the colors in Figure 9 schematically denote this difference in temperature: red and yellow are for higher temperatures and green and blue are for lower ones.

Furthermore, those snapshots also indicate that the separatrix bubble above the current sheet grows much faster in both size and height than the corresponding flare loop system below the current sheet. This is because the flare loops occur in the lower corona, with strong magnetic field and dense plasma compared to the upper corona, in which the separatrix bubble propagates and expands. The tenuous plasma and weak magnetic field in the outermost corona and interplanetary space make it fairly easy for the separatrix bubble to grow. Comparing the curves in Figure 8*c* with the solid curve in Figure 6*g* of Lin (2002) provides us with more quantitative understanding of the differences in sizes and evolutionary behaviors between CMEs and flare loops. Interested readers may also refer to Švestka (1996), Ko et al. (2003), and Lin (2002) for more discussions and observational evidence.

4.2. *Implications for Observed Features in Eruptive Processes*

Although our calculation is in two dimensions, the snapshots in Figure 9 could be considered as cross sections of a three-

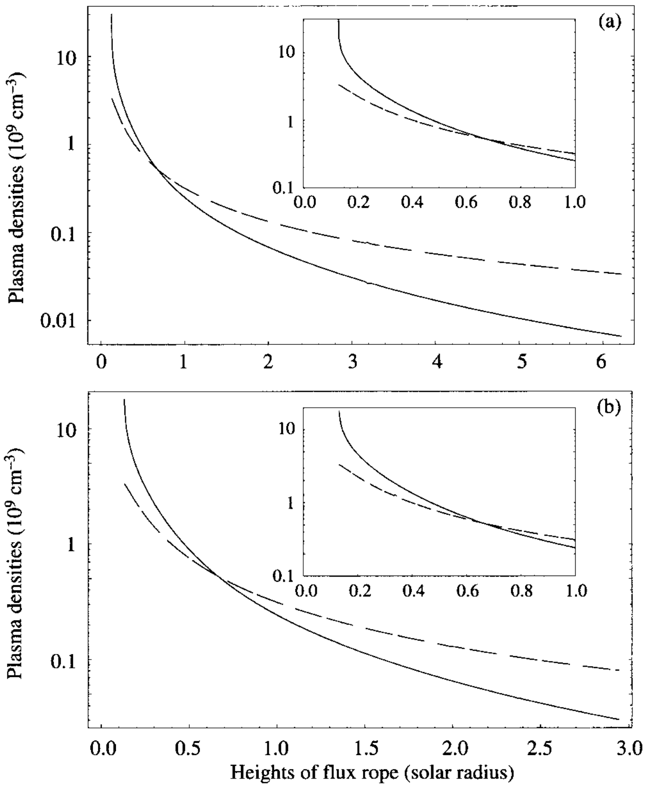

FIG. 10.—Variations of the average densities of the plasma inside the separatrix bubble vs. height of flux rope for (*a*) $B_0 = 100$ G and (*b*) $B_0 = 50$ G. The solid curves are for the plasma in the volume surrounded by S_1 and S_i at $t = t_i$, where $i = 2, 3, \ldots$, and the dashed curves for the plasma inside S_1 (the plasma inside the flux rope is not included). Also refer to Fig. 11.

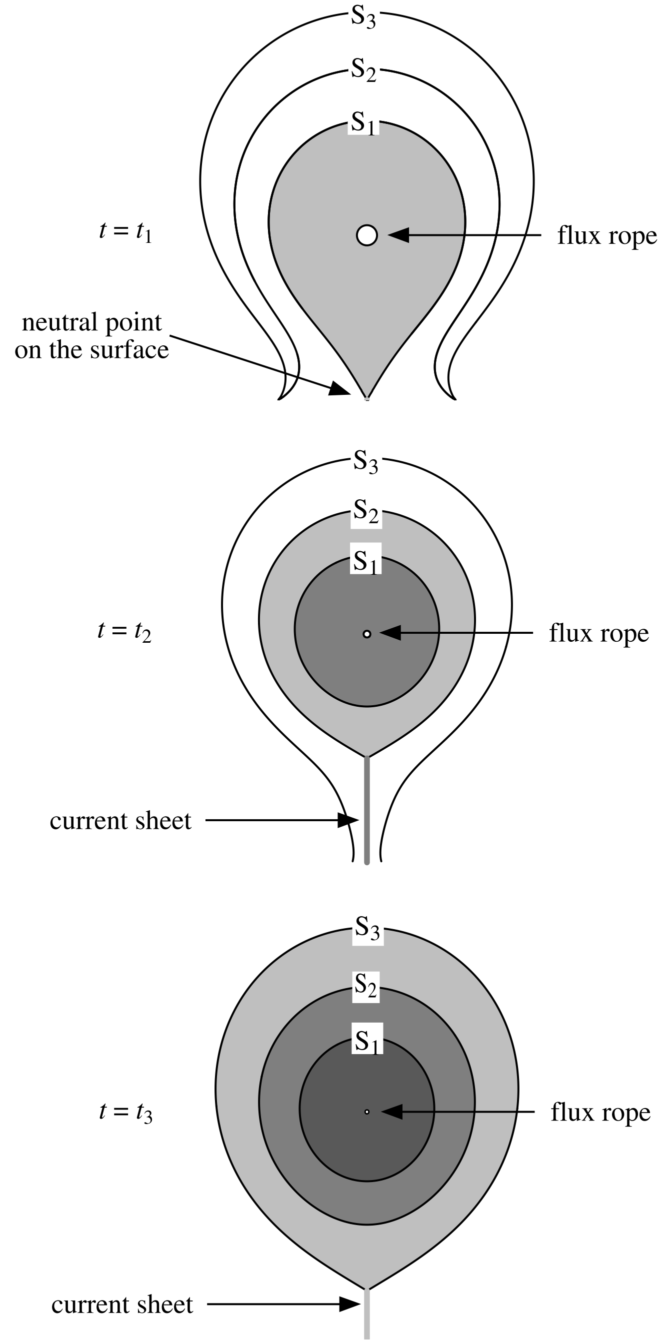

FIG. 11.—Schematic descriptions of the evolution of the separatrix bubble in the eruptive process for $t = t^* = t_1$ (*top*), $t = t_2$ (*middle*), and $t = t_3$ (*bottom*). To specify features of the separatrix, the three panels are not plotted in same scale.

dimensional configuration that includes a flux rope with two ends anchored in the photosphere. The evolutionary behavior of the disrupted magnetic field revealed by those snapshots still predicts some valuable observational consequences. Because of the rapid growth of the bubble and the insufficient supply of plasma, the average density inside the bubble decreases quickly with time, and the bubble fades rapidly as it propagates through the outer corona and interplanetary space. However, fresh material is continually injected at the outer edge of the bubble, so a limb-brightened structure may be seen.

Figure 10 demonstrates variation of the average density of the plasma inside the bubble, $\bar{n}$, versus the flux rope altitude, h, for two different background fields, B_0. The dashed curves describe the plasma densities inside the volume surrounded by the separatrix, S_1, defined at the moment, $t = t_1 = t^*$, when a neutral point appears on the boundary surface and a current sheet starts to develop. The solid curves show the densities of the plasma in the volume outside S_1 and inside the new separatrix S_i at time $t = t_i > t^*$, where $i = 2, 3, \ldots$ (see Fig. 11).

At time $t = t^*$, when magnetic reconnection begins in the reconnection site, the separatrix bubble surrounded by S_1 does not contain the plasma flowing from the reconnection site, but only that preexisting in the coronal background. As magnetic reconnection continues, S_1 detaches from the current sheet. As a result of the frozen-in condition, the total amount of plasma inside S_1 does not change subsequently. At time $t = t_2$, field line S_2 attaches to the current sheet and becomes the new separatrix. Progressive reconnection drives the separatrix from one field line, S_1, to another one, S_2, and then to another one, S_3, and so on. (Fig. 11).

As a result of the freezing-in of plasma to magnetic field, the plasma flowing out of the current sheet is guided by the separatrix and fills a thin layer around the separatrix. The plasma density in this layer is a function of time and altitude. For $B_0 = 100$ G, Figure 12 shows the densities at three positions in the bubble compared to the pre-CME densities at those heights. As denoted in Figure 2, position B is at the top of the bubble, C is at the edge of the bubble at the same height as the flux rope center, and D is at the upper tip of the current sheet. Each labeled curve in Figure 12 plots the corresponding density change against the height of flux rope h. Note that the density is assumed to be the same at all three locations in the

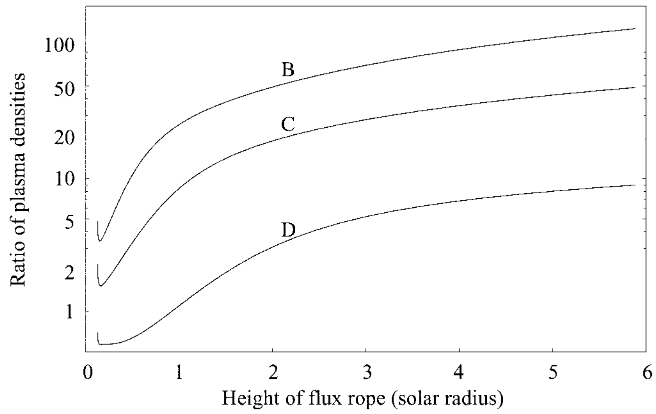

FIG. 12.—Variations of the relative plasma densities in the outer shell of the separatrix bubble vs. the corresponding altitude of flux rope h ($B_0 = 100$ G).

bubble, but the density of the pre-CME corona varies by an order of magnitude among those heights. The behavior of each curve at its lower end may be because of the fact that the amount of plasma injected into the bubble at low altitudes increases more slowly than the volume of the bubble.

We suggest that the dense shell at the outer edge of the bubble may correspond to the leading edge in the classic three-part structure of CMEs (Hundhausen et al. 1994; Low 2001). It is also possible that compressed plasma ahead of the bubble accounts for the bright leading edge, especially in CMEs that produce shocks. More detailed computations will be needed to elucidate the relative contributions of compression ahead of the CME and plasma flow into the outer bubble from the current sheet. The CME bubble expands rapidly, so that the average density inside the bubble is lower than that inside the outer shell of the bubble. Thus, the bubble can be naturally identified with the CME void. Finally, the plasma inside the original flux rope, which is used to model the prominence in catastrophe model of CMEs, is initially in the range from 10^{11} to $\sim 10^{12}$ cm^{-3} (see Jensen, Maltby, & Orrall 1979, Tandberg-Hanssen 1974, and Priest 1982), and this can be identified with the CME core.

More detailed computations will be required to confirm the proposed identifications. In particular, we have simply assumed that plasma is injected into the outer shell of the bubble at a speed high enough that it is evenly distributed around the shell. A more modest injection speed would lead to a lower density at the CME front and a U- or V-shaped structure at the top of the current sheet. U- or V-shaped structures are observed in at least 10% of CMEs and are generally classed as coronal disconnection events (Webb et al. 2003). More detailed computations will also help to clarify the amount of heating that occurs and whether the injected plasma ought to appear in high-temperature lines, such as [Fe XVIII], as observed in some fast CMEs (Raymond et al. 2003).

5. CONCLUSIONS AND DISCUSSION

We propose a CME model in which plasma and magnetic flux are brought from the high corona into the heliosphere by magnetic reconnection in a current sheet developing behind the erupting flux rope. Our calculation indicates that the reconnected plasma and magnetic flux propagate together with the ejecta (or the flux rope in the framework of our model). The reconnected plasma and magnetic flux are very much like the structures predicted by CME models that do not begin with a flux rope, and it may be difficult to distinguish between models based on observations at large heights. In either model, however, the mass, speed, amount of magnetic flux, and direction of the magnetic field around the flux rope are determined as the CME propagates through the region a few solar radii above the photosphere, and these are the quantities that determine the geoeffectiveness of a CME.

The main results are summarized as follows:

1. Like the flare/CME loop/giant arch system, the separatrix bubble that surrounds the flux rope, together with the hot plasma inside, is the product of magnetic reconnection. As magnetic reconnection sends more and more plasma and magnetic flux into the separatrix bubble, the bubble swells very rapidly (i.e., much faster than a flux rope). The "flux rope" that is often observed by coronagraphs may actually be the rapidly expanding separatrix bubble.
2. The magnetic flux ejected into the heliosphere by CMEs consists of two components. One is due to the toroidal magnetic field and the other due to the poloidal field. The flux contributed by the toroidal field mainly exists in the flux rope prior to the eruption. For the model presented in § 3, the value of the magnetic flux due to the toroidal field is 6.53×10^{20} Mx, while the values estimated according to the observational data of Lepping et al. (1990, 1997) and Webb et al. (2000) range from 4.55×10^{20} to 1.46×10^{22} Mx. As for the magnetic flux due to the poloidal field, the present work indicates that there are several sources, but observations are not able to distinguish one from another. An in situ measurement provides a total amount of the poloidal flux from all the sources, which varies from 3.35×10^{21} to 2.68×10^{22} Mx, while our calculation gives a few times 10^{22} Mx.
3. The outflow of reconnected plasma and magnetic flux leaves the reconnection site through both tips of the current sheet. The downward flow finally reaches the chromosphere and causes the latter to evaporate, creating bright flare loops and ribbons. The upward flow is eventually sealed in the separatrix bubble, creating a rapidly expanding structure that observers usually identify as the flux rope. The plasma in the upward flow fills the outer shell of the separatrix bubble and probably causes the separatrix bubble to show the three-component feature of CMEs. On the other hand, comparison with observations also indicates that more rigorous investigations of the three-component structure are needed.

We have investigated various observational consequences based on a catastrophe model of the solar eruptions, primarily those accessible to white light coronagraphs involving density and velocity. Heating is another consequence of the model, although there is still no robust way to tell how the energy dissipated by reconnection is divided between heat and kinetic energy. Recent work by Filippov & Koutchmy (2002), Ciaravella et al. (2000, 2001), and Akmal et al. (2001) points to strong heating in CMEs at heights of a few solar radii. It is not obvious that the plasma injected by the current sheet can reach the prominence material in the original flux rope with the form sketched in Figure 1. However, if the field lines inside flux rope are sufficiently tangled, there might be some internal reconnection as the flux rope evolves toward a constant-α Lundquist solution (refer to eq. [4]). This can, in principle, provide both heating and some mixing of hot and cool plasma within the interplanetary CME.

The authors appreciate the referee's valuable comments and suggestions. This work was supported by NASA under grants NAG5-12865 and NAG5-12827 to the Smithsonian Astrophysical Observatory.

APPENDIX

CONSERVATION OF TOROIDAL FLUX $\Phi_{\rm tor}$

The magnetic induction equation for a cylindrical flux rope can be written in the form

$$\frac{\partial B_\phi}{\partial t} = \frac{\partial}{\partial r}\left[-V_r B_\phi + \frac{\eta}{r}\frac{\partial}{\partial r}\left(rB_\phi\right)\right], \tag{A1}$$

$$\frac{\partial B_z}{\partial t} = \frac{1}{r}\frac{\partial}{\partial r}\left[-rV_r B_z + r\eta\frac{\partial B_z}{\partial r}\right], \tag{A2}$$

where $V_r(r, t)$ is the radial velocity and $\eta(r)$ is the magnetic diffusivity of the coronal plasma. The expression in square brackets in equation (A2) vanishes for $r \rightarrow 0$. This implies that the toroidal flux $\Phi_{\rm tor}$ is conserved (constant in time) even in the presence of magnetic diffusion within the flux rope. However, the poloidal flux $\Phi_{\rm pol}$ is not conserved, because the term $r^{-1}\partial\left(rB_\phi\right)/\partial r$ in equation (A1) approaches a nonzero value in the limit $r \rightarrow 0$. Therefore, we expect the toroidal flux to remain unchanged as the CME expands into the heliosphere, but the poloidal flux may decrease as a result of the resistive diffusion within the flux rope.

REFERENCES

Akmal, A., Raymond, J. C., Vourlidas, A., Thompson, B., Ciaravella, A., Ko, Y.-K., Uzzo, M., & Wu, R. 2001, ApJ, 553, 922

Amari, T., Luciani, J. F., Aly, J. J., Mikić, Z., & Linker, J. 2003, ApJ, 585, 1073

Amari, T., Luciani, J. F., Mikić, Z., & Linker, J. 2000, ApJ, 529, L49

Antiochos, S. K., DeVore, C. R., & Klimchuk, J. A. 1999, ApJ, 510, 485

Aulanier, G., Srivastava, N., & Martin, S. F. 2000, ApJ, 543, 447

Burlaga, L. F. 1988, J. Geophys. Res., 93, 7217

Carmichael, H. 1964, in The Physics of Solar Flares, ed. W. N. Hess (Washington: NASA), 451

Choe, G. S., & Lee, L. C. 1992, Sol. Phys., 138, 291

Ciaravella, A., Raymond, J. C., Li, J., Reiser, P., Gardner, L. D., Ko, Y.-K., & Fineschi, S. 2002, ApJ, 575, 1116

Ciaravella, A., Raymond, J. C., Reale, F., Strachan, L., & Peres, G. 2001, ApJ, 557, 351

Ciaravella, A., et al. 2000, ApJ, 529, 575

Farrugia, C. J., Burlaga, L. F., & Lepping, R. P. 1997, in Magnetic Storms, ed. B. T. Tsurutani, W. D. Gonzales, Y. Kamide, & J. K. Arballo (Geophys. Monogr. 98; Washington: AGU), 91

Filippov, B., & Koutchmy, S. 2002, Sol. Phys., 208, 283

Forbes, T. G. 2000a, Philos. Trans. R. Soc. London, A 358, 711

———. 2000b, J. Geophys. Res., 105, 23153

Forbes, T. G., & Acton, L. W. 1996, ApJ, 459, 330

Forbes, T. G., & Isenberg, P. A. 1991, ApJ, 373, 294

Forbes, T. G., & Lin, J. 2000, J. Atmos. Sol.-Terr. Phys., 62, 1499

Forbes, T. G., & Priest, E. R. 1995, ApJ, 446, 377

Gibson, S. E., & Low, B. C. 1998, ApJ, 493, 460

Gibson, S. E., et al. 2002, ApJ, 574, 1021

Goldstein, H. 1983, in Solar Wind Five, ed. M. Neugebauer (NASA CP-2280; Washington: NASA), 731

Gosling, J. T. 1993, J. Geophys. Res., 98, 18937

Harrison, R. A. 1996, Sol. Phys., 166, 441

———. 1997, in Correlated Phenomena at the Sun, in the Heliosphere, and in Geospace, ed. A. Wilson (ESA-SP 415; Noordwijk: ESA), 121

Harrison, R. A., Bryans, P., Simnett, G. M., & Lyons, M. 2003, A&A, 400, 1071

Harrison, R. A., & Lyons, M. 2000, A&A, 358, 1097

Howard, R. A., Sheeley, N. R., Jr., Michels, D. J., & Koomen, M. J. 1985, J. Geophys. Res., 90, 8173

Howard, R. A., et al. 1997, in Coronal Mass Ejections, ed. N. Crooker, J. A. Joselyn, & J. Feynman (Geophys. Monogr. 99; Washington: AGU), 17

Hundhausen, A. J., Stanger, A. L., & Serbicki, S. A. 1994, in Solar Dynamic Phenomena and Solar Wind Consequences, ed. J. J. Hunt (ESA-SP 373; Noordwijk: ESA), 409

Inhester, B., Birn, J., & Messe, M. 1992, Sol. Phys., 138, 257

Jensen, E., Maltby, P., & Orrall, F. Q., ed. 1979, IAU Colloq. 44, Physics of Solar Prominences (Oslo: Inst. Theor. Astrophys.)

Ko, Y.-K., Raymond, J. C., Lin, J., Lawrence, G., Li, J., & Fludra, A. 2003, ApJ, 594, 1068

Kopp, R. A., & Pneuman, G. W. 1976, Sol. Phys., 50, 85

Krall, J., Chen, J., & Santoro, R. 2000, ApJ, 539, 964

Lepping, R. P., Jones, J. A., & Burlaga, L. F. 1990, J. Geophys. Res., 95, 11957

Lepping, R. P., Szabo, A., DeForest, C. E., & Thompson, B. J. 1997, in Correlated Phenomena at the Sun, in the Heliosphere, and in Geospace, ed. A. Wilson (ESA-SP 415; Noordwijk: ESA), 163

Lin, J. 2001, Ph.D. thesis, Univ. New Hampshire

———. 2002, Chinese J. Astron. Astrophys., 2, 539

Lin, J., & Forbes, T. G. 2000, J. Geophys. Res., 105, 2375

Lin, J., Forbes, T. G., & Isenberg, P. A. 2001, J. Geophys. Res., 106, 25053

Lin, J., Forbes, T. G., Isenberg, P. A., & Démoulin, P. 1998, ApJ, 504, 1006

Lin, J., Forbes, T. G., Priest, E. R., & Bungey, T. N. 1995, Sol. Phys., 159, 275

Lin, J., Soon, W., & Baliunas, S. L. 2003, NewA Rev., 47, 53

Lin, J., & van Ballegooijen, A. A. 2002, ApJ, 576, 485

Lin, J., van Ballegooijen, A. A., & Forbes, T. G. 2002, J. Geophys. Res., 107(A12), 1438

Lin, J., & Wang, J. X. 2002, in Solar-Terrestrial Magnetic Activity and Space Environment, ed. H. Wang & R. Xu (Boston: Pergamon), 137

Lites, B. W., Low, B. C., Martínez Pillet, V., Seagraves, P., Skumanich, A., Frank, Z. A., Shine, R. A., & Tsuneta, S. 1995, ApJ, 446, 877

Low, B. C. 2001, J. Geophys. Res., 106, 25141

Lundquist, S. 1950, Ark. Fys., 2, 361

Mackay, D. H., & van Ballegooijen, A. A. 2001, ApJ, 560, 445

Manchester, W., IV 2003, J. Geophys. Res., 108(A4), 1162

Marubashi, K. 1986, Adv. Space Res. 6(6), 335

Mikić, Z., Barnes, D. C., & Schnack, D. D. 1988, ApJ, 328, 830

Mikić, Z., & Linker, J. A. 1994, ApJ, 430, 898

Parker, E. N. 1974, ApJ, 191, 245

Priest, E. R. 1982, Solar Magnetohydrodynamics (Boston: Reidel), 127

Priest, E. R., & Forbes, T. G. 2002, A&A Rev., 10, 313

Raymond, J. C., Ciaravella, A., Dobrzycka, D., Strachan, L., Ko, Y.-K., Uzzo, M., & Raouafi, A.-E. 2003, ApJ, 597, 1106

Roussev, I. I., Forbes, T. G., Gombosi, T. I., Sokolov, I. V., DeZeeuw, D. L., & Birn, J. 2003, ApJ, 588, L45

Schmieder, B., Forbes, T. G., Malherbe, J. M., & Machado, M. E. 1987, ApJ, 317, 956

Sittler, E. C., Jr., & Guhathakurta, M. 1999, ApJ, 523, 812 (erratum 564, 1062 [2002])

Sterling, A. C., & Hudson, H. S. 1997, ApJ, 491, L55

Švestka, Z. 1996, Sol. Phys., 169, 403

Švestka, Z., & Cliver, E. W. 1992, in Eruptive Solar Flares, ed. Z. Švestka, B. V. Jackson, & M. E. Machado (New York: Springer), 1

Švestka, Z., & Fárník, F. 1998, in Observational Plasma Astrophysics: Five Years of *Yohkoh* and Beyond, ed. T. Watanabe, T. Kosugi, & A. C. Sterling (Boston: Kluwer), 365

Švestka, Z., Fárník, F., Hick, P., Hudson, H. S., & Uchida, Y. 1997, Sol. Phys., 176, 355

Tandberg-Hanssen, E. 1974, Solar Prominences (Dordrecht: Reidel)

Thompson, B. J., Cliver, E. W., Nitta, N., Delannée, C., & Delaboudinière, J. P. 2000, Geophys. Res. Lett., 27, 1431

van Ballegooijen, A. A., & Martens, P. C. H. 1989, ApJ, 343, 971

van Ballegooijen, A. A., Priest, E. R., & Mackay, D. H. 2000, ApJ, 539, 983

Vourlidas, A., Subramanian, P., Dere, K. P., & Howard, R. A. 2000, ApJ, 534, 456
Wang, J. 1998, in ASP Conf. Ser. 140, Synoptic Solar Physics, ed. K. S. Balasubramaniam, J. Harvey, & D. Rabin (San Francisco: ASP), 121
———. 1999, Fundam. Cosmic Phys., 20, 251
Webb, D. F. 2000, IEEE Trans. Plasma Sci., 28, 1795
Webb, D. F., Burkepile, J., Forbes, T. G., & Riley, P. 2003, J. Geophys. Res., 108(A12), 1440
Webb, D. F., Howard, R. A., & Jackson, B. V. 1996, in AIP Conf. Proc. 382, Solar Wind Eight, ed. D. Winterhalter, J. T. Gosling, S. R. Habbal, W. S. Kurth, & M. Neugebauer (Woodbury: AIP), 540
Webb, D. F., Lepping, R. P., Burlaga, L. F., DeForest, C. E., Larson, D. E., Martin, S. F., Plunkett, S. P., & Rust, D. M. 2000, J. Geophys. Res., 105, 27251
Wu, S. T., Guo, W. P., & Dryer, M. 1997, Sol. Phys., 170, 265
Zarro, D. M., Sterling, A. C., Thompson, B. J., Hudson, H. S., & Nitta, N. 1999, ApJ, 520, L139